



Morphology-controlled metal–organic frameworks as molecular traps for enhanced ion dynamics in practical semi-solid lithium metal batteries

Daero Lee^{a,1}, Kyeong-Seok Oh^{a,1}, Yeongkyu Lee^{b,c}, Jie Jin^a, Sang-Young Lee^{a,*},
Yongseok Jho^{b,*}, Jong Hyeok Park^{a,*}

^a Department of Chemical and Biomolecular Engineering, Yonsei University, 50 Yonsei-ro, Seodaemun-gu, Seoul 03722, Republic of Korea

^b Department of Physics and Research Institute of Molecular Alchemy, Gyeongsang National University, 11 (GNU), 501 Jinju-daero, Jinju 52828, Republic of Korea

^c School of Computational Sciences, Korea Institute for Advanced Study, 85 Hoegi-ro, Dongdaemun-gu, Seoul 02455, Republic of Korea

ARTICLE INFO

Keywords:

Metal–organic frameworks
Morphology-controlled electrolytes
Anion immobilization
Lithium-ion boosting molecular traps
Semi-solid lithium metal batteries

ABSTRACT

Controlling electrostatic interactions between charged molecules is crucial to enabling advanced batteries with reliable lithium (Li)-ion conductors. To address this issue, herein, we present a class of morphology-controlled metal–organic frameworks (MOFs) that serve as Li⁺ boosting molecular traps for fast Li⁺ conduction. A rod-like MOF is incorporated into semi-interpenetrating polymer networks to construct Li⁺ boosting fluidic nano-channels, which enable fast Li⁺ transport ($\sigma = 1.5 \text{ mS cm}^{-1}$, $t_{\text{Li}^+} = 0.76$) through the ionic pathway. Molecular dynamics simulations further elucidate the Li⁺ transport mechanism in these MOF-based molecular traps. This unusual Li⁺ conduction behavior of MOF-based semi-solid electrolytes suppresses the anion-triggered ion concentration gradient and facilitates the electrochemical reaction kinetics at the electrodes, ultimately improving the rate performance and cycling retention of Li-metal cells (consisting of LiNi_{0.7}Co_{0.2}Mn_{0.1}O₂ cathodes and Li-metal anodes). Notably, a scalable pouch-type semi-solid Li-metal cell provides stable cycling performance for realistic batteries, exceeding those of previously reported Li batteries including porous crystalline frameworks.

1. Introduction

As the smart energy era dawns, the demand for high-energy density power sources with reliable electrochemical performance, processability, and safety is rapidly growing for smart portable electronics, electric vehicles (EVs), grid-scale energy storage systems (ESSs), and the Internet of Things (IoT) [1–3]. Among the numerous next-generation battery systems explored to date, solid-state lithium (Li) batteries with Li-metal anodes have been extensively investigated as promising post Li battery candidates [4–6]. Such a great interest in these batteries inspires the relentless pursuit of solid-state Li⁺ conductors as a key enabling technology [7–9].

Previous studies on the solid-state ion conductors have focused on inorganic-based and polymer-based electrolytes [10–12]. For inorganic-based electrolytes such as sulfide/oxide, high Li⁺ conductivities (namely, ion conductivity multiplied by Li⁺ transference number (t_{Li^+}), 1–10 mS cm^{−1}, $t_{\text{Li}^+} = 1$) have been revealed at room temperature [13–15]. However, their dependence on advanced fabrication methods

(e.g., atomic layer deposition) to form low interfacial resistances with the electrodes has hindered their further development with undergoing high-pressure/high-temperature manufacturing steps [16–18]. In contrast, solid polymer electrolytes (SPEs) such as polyethylene oxides have been limited to their operation at only elevated temperatures (60–80 °C) due to low bulk Li⁺ conductivities (< 0.1 mS cm^{−1}, $t_{\text{Li}^+} < 0.4$) at room temperature despite their high flexibility, light weight, low cost, and ease of processing [19,20].

So far, considerable efforts have been made to overcome these problems of SPEs, with particular attention paid to the incorporation of inorganic fillers [21–23]. Among the various inorganic fillers, active fillers (i.e., perovskite, garnet, LISICON, etc.) are attracting increasing attention due to their superior Li⁺ conductivities [24,25]. However, conventional active fillers cannot rectify anion movement, and freely movable anions cause concentration polarization, unwanted side reactions with electrodes, and dendritic Li growth, which hinder the widespread application of SPEs in Li-metal batteries (LMBs) [26].

Metal-organic frameworks (MOFs) have shown great potential for

* Corresponding authors.

E-mail addresses: syleek@yonsei.ac.kr (S.-Y. Lee), ysjho@gnu.ac.kr (Y. Jho), lutts@yonsei.ac.kr (J.H. Park).

¹ These authors contributed equally.

the fabrication of high-performance SPEs due to their tunable properties, such as pore size, porosity, and polarity, which can provide systematic modularity for effective Li^+ transport [27–29]. Recently, 2D MOF nanosheets have attracted attention due to their enhanced ionic conductivity and large contact area with the polymer matrix, which increase the number of active sites and provide many opportunities for targeted functional design [30,31]. However, the preparation of active MOF fillers often requires immersion of MOF particles in liquid electrolyte (LE) or ionic liquid followed by vacuum drying, which is a discontinuous, time-consuming process [32]. Furthermore, due to the difficulty in controlling the size, shape, and growth of MOFs, previous studies have focused on finite MOF morphologies, and the importance of their dimensions for Li^+ transport has not been fully investigated. Systematic designs are essential to elucidate the correlation between morphology and Li^+ transport behavior in MOF-based SPEs. The variation in filler morphologies holds the potential to significantly improve the performance of SPEs [33].

Here, we address the aforementioned challenges of SPEs by developing a new class of morphology-controlled MOFs that serve as Li^+ boosting molecular traps in semi-interpenetrating polymer networks (semi-IPNs) via an *in-situ* ultraviolet (UV)-curing process. Among various MOFs, bismuth MOFs were chosen due to their intricate three-dimensional crystalline porous framework structures and tunable morphology, which maximize Li^+ transport through systematic design. To further improve the Li^+ transport in SPEs by morphology modification of MOFs, two types of bismuth MOFs (CAU-17 sheets and CAU-17 rods) were designed by modulating the growth direction and incorporated into the semi-IPN structure of a 3D cross-linked polymer network and linear polymer. The Li^+ transport efficiency of MOF-incorporated SPE is significantly enhanced by the morphological modification of CAU-17, from sheets ($\sigma_{\text{Li}} = 0.52 \text{ mS cm}^{-1}$) to rods ($\sigma_{\text{Li}} = 1.14 \text{ mS cm}^{-1}$), which can outperform pristine SPE without MOF molecular traps ($\sigma_{\text{Li}} = 0.35 \text{ mS cm}^{-1}$). The high Li^+ transference number was attributed to the anion-immobilization ability of open metal sites (OMS) in the MOF pores, which reduces the concentration polarization and suppresses the formation of Li dendrites. Furthermore, the anchored anions regulated the Li^+ transport in the MOF pore, which was elucidated by molecular dynamics (MD) simulations.

Compared with inorganic electrolytes such as sulfides and oxides, MOF-based SPE easily formed intimate contact with the electrodes and can be paired with commercially available $\text{LiNi}_{0.7}\text{Co}_{0.1}\text{Mn}_{0.2}\text{O}_2$ (NCM712) cathode without further cell engineering. Semi-solid Li-metal-batteries (SSLMBs) that are composed of a Li-metal anode and a NCM712 cathode utilizing CAU-17 rods exhibited stable charge/discharge performance over a wide range of C-rate (0.2 C to 10.0 C). In addition, we fabricated a pouch-type cell to explore the practical viability of the MOF molecular traps, which exhibited stable cycling performance (86.7% after 100 cycles) even at high C-rate, far exceeding those of previously reported SSLMB cells based on porous crystalline frameworks. This work presents a novel design of the MOF platform with a comprehensive study to understand the relationship between the morphologies and the Li^+ transport behavior in the SPE-based SSLMBs.

2. Experimental section

2.1. Preparation of bismuth MOFs

Bismuth MOFs were synthesized via hydrothermal treatment, following the methodology outlined in a prior study [34]. Subsequently, CAU-17 rods were produced using the described synthesis protocol. H_3BTC (500 mg) and $\text{Bi}(\text{NO}_3)_3 \cdot 5\text{H}_2\text{O}$ (150 mg) were mixed in 40 mL of methanol (MeOH) at room temperature until the chemicals were dissolved. This solution was then sealed, placed in an autoclave and heated to 120 °C for 24 h. Finally, the MOF powder was separated by centrifugation and washed three times with MeOH. The as-obtained sample was dried in a vacuum oven at 120 °C for 12 h. The CAU-17 with sheet

morphology were prepared by the same hydrothermal method, except that the mixture of $\text{Bi}(\text{NO}_3)_3 \cdot 5\text{H}_2\text{O}$ (150 mg) and H_3BTC (500 mg) was stirred for 20 min until sediment was formed, and the other conditions were the same as those used for the preparation of the CAU-17 rods.

2.2. Preparation of the solid-state organic electrolyte precursor

A series of bismuth MOFs were added to liquid electrolyte (1 M LiPF_6 in ethylene carbonate (EC)/diethyl carbonate (DEC) = 1/1 (v/v), Soulbrain Co.) and sonicated for 30 min to disperse the MOF particles in the solution. Then, UV-curable ethoxylated trimethylolpropane triacrylate (ETPTA) monomer ($M_w = 428$, Sigma-Aldrich), 2-hydroxy-2-methylpropiophenone photoinitiator (HMPP, Sigma-Aldrich) and polyvinylidene fluoride-co-hexafluoropropylene (PVdF-HFP) (Kynar 2801, HFP content: 12 mol.%) were then added to the solution and stirred for 24 h to form a homogeneous mixed precursor. The weight ratio of ETPTA/PVdF-HFP was 70/30, and that for the semi-IPN polymer matrix/liquid electrolyte was 10/90. The concentration of MOFs added ranged from 0 to 4% by weight of the polymer matrix. The concentration of the HMPP photoinitiator was 5 wt.% relative to the polymer matrix.

2.3. Molecular dynamics simulations in detail

MD simulations were conducted to determine the Li^+ and PF_6^- kinetics in the CAU-17 pores. We took the structure of CAU-17 from previous work reported by Inge *et al* [35]. Lennard–Jones (LJ) potentials for the atoms were taken from prior study [36]. We calculated the partial charges of the system by using the GAUSSIAN-16 quantum calculation package based on the Millikan charge method [37]. The forcefield parameters for EC, DEC, Li^+ , and PF_6^- were taken from the OPLS-AA forcefield [38]. For Li^+ and PF_6^- , we scaled the partial charges to mimic the polarization properties in a nonpolarizable forcefield [39].

The system consisted of EC and DEC solvents. As the salt, Li^+ and PF_6^- were added. The concentration ratio for solvents and salts was $M_{\text{salts}}: M_{\text{EC}}: M_{\text{DEC}} \approx 1:7:4$. We placed these molecules in a pore of the CAU-17 after calculating the volume of the pore. The positions of the CAU-17 atoms were fixed during the simulations. Simulations of the whole unit cell of CAU-17 are computationally too expensive. Instead, we simulated a part of the pore, as single pore is enough for our purpose to study the dynamics of salts and solvents inside the pore of CAU-17. We modeled the pore with a 1 D periodicity on the z-axis. Solvents were filled both inside and outside of the pore. To compare the transport properties of the pore with those of the bulk, we prepared a bulk system consisting of solvents and salts. We placed solvents and salts in a cubic box by matching the concentration ratio of the molecules as mentioned above. Initial configurations for the MD simulations were prepared by the PACKMOL package, which can easily build the initial structures for MD simulations. We used the GROMACS package to run the MD simulations [40]. Energy minimization was conducted by using the steepest descent algorithm. We ran a canonical ensemble simulation to relax the system at a high temperature (500 K) for 100 ps and equilibrated the system at the target temperature (300 K) for 1 ns. The time steps for equilibration and relaxation were 1 fs. The production run followed the NVT ensemble for hundreds of nanoseconds at 300 K.

In the experiment, there is an external electric field through the pore. We extracted the free diffusion part of ion motion by removing the trending part generated by the electric field. In the simulation, we also applied the corresponding external field to mimic it. Then, the overall ion motion will combine both drift and diffusion. We extract the free diffusion part of the mean squared displacements (MSDs) by removing the drift term. Because the drift motion is linearly dependent on the external field, the detrended analysis will strip away the drift part. Then, detrended MSD is the time correlation of the fluctuation part only, $\langle \xi(t)\xi(t_0) \rangle$. Auto-correlation function measures $C(t) = \langle h(t)h(0) \rangle$. The indicator function $h(t)$ has 1 if the solvation shell does not change during the time t . Otherwise, it is 0. We analyzed the position differences

$d\mathbf{r} = |\mathbf{r}(t) - \mathbf{r}(t_0)|$ as a function of time for free and bound states of Li^+ and PF_6^- .

Two states are classified using a quantity called P_{hop} , defined by

$$P_{\text{hop}} = \sqrt{\sigma_A \sigma_B} \quad (1)$$

where A and B denote the time intervals $A = [t - \tau, t]$ and $B = [t, t + \tau]$, respectively [41,42]. And τ is a time-scale for exchange duration, $\sigma_A = \langle (\gamma_i - \langle \gamma_i \rangle_B)^2 \rangle_A$ and $\sigma_B = \langle (\gamma_i - \langle \gamma_i \rangle_A)^2 \rangle_B$. $\langle \dots \rangle$ denotes the time average for intervals A and B . P_{hop} detects hopping-like motions of caged or bound ions. σ_A (or σ_B) refers to the deviation of particle position, so it is similar to the size of the caged or bound potential well. If a particle escapes its bound state, the P_{hop} is large. We collected the distribution of P_{hop} at escapes and chose the cutoff level of P_{hop} to embrace most escape events.

2.4. Cell assembly

The positive electrode was prepared by mixing NCM712 (L&F Co.), carbon black (Super-P), and polyvinylidene fluoride (Kynar, HSV900) in *N*-methyl-2-pyrrolidone (NMP, Sigma-Aldrich) solvent in a weight ratio of 80:10:10, coating it on aluminum foil, and then drying it at 110 °C in a vacuum oven for 8 h. The NCM712 cathode loading was adjusted to give an areal capacity of approximately 1 mAh cm⁻². The precursor prepared above, 100 μL , was injected onto the positive electrode placed on the case, and a polyethylene (PE) separator was placed inside, followed by UV irradiation for 30 s with a UV lamp to cure the electrolyte (UV cure-60PH, Lichtzen). All 2032 coin cells were assembled in an argon-filled glove box. Li-metal (Hohsen) was used as a reference/counter electrode to test the electrochemical performance. A pouch-type cell was fabricated (length \times width = 20 \times 20 (mm \times mm)). The pouch-type cells were sealed with an Al pouch as a packaging substance. All pouch-type cells were assembled in a dry room at room temperature and ambient pressure.

2.5. Characterization and measurements

Nitrogen adsorption tests were conducted for each synthesized sample using an Autosorb-iQ 2ST/MP system (Quantachrome) and based on the Brunauer-Emmett-Teller (BET) theory. Nitrogen adsorption was measured at liquid nitrogen temperature (77 K), and all samples were thermally treated at 300 °C prior to measurement. The sizes and distributions of micropores and mesopores were analyzed using the Barrett-Joyner-Halenda (BJH) theory. Field emission-scanning electron microscope (FE-SEM) equipped with an energy-dispersive X-ray spectroscopy (EDS) was used to observe the surface and cross-sectional morphologies of the electrolytes (JEOL-7800F, JEOL Ltd.). The thermal cross-linking reactions of the electrolytes were monitored by a Fourier transform infrared (FT-IR) spectrometer (Vertex70, Bruker) scanning in the range of 4000–600 cm⁻¹. X-ray diffraction (XRD) patterns of the samples were obtained with a SmartLab (Rigaku) analyzer. Thermogravimetric analysis (TGA) was carried out using a Q50 instrument (TA Instruments). Each sample was placed in a platinum pan and heated from 30 to 600 °C with a ramping rate of 10 °C min⁻¹ in a nitrogen atmosphere. The glass transition temperature of each polymer was measured by differential scanning calorimetry (DSC) according to ASTM D4065 at a heating rate of 10 °C min⁻¹. X-ray photoelectron spectroscopy (XPS) analysis was conducted to examine the SEI layer of Li the metal (K-alpha, Thermo Scientific Inc., U.K.).

2.6. Electrochemical measurements

The ionic conductivities (σ) of the electrolytes were tested by AC impedance spectroscopy (CHI-660, CH Instruments) with the electrolyte sandwiched between stainless steel (SUS) electrodes, and the conductivities were calculated as follows:

$$\sigma = \frac{t}{(A \times R_b)} \quad (2)$$

where A is the area in contact with the electrodes, R_b is the bulk resistance of the electrolyte, and t is the thickness of the electrolyte. The t_{Li^+} was measured by chronoamperometry/AC impedance spectra with symmetric Li-metal coin cells and calculated using the following equation:

$$t_{\text{Li}^+} = \frac{I_s(\Delta V - I_0 R_0)}{I_0(\Delta V - I_s R_s)} \quad (3)$$

where I_0 and I_s are the initial and steady-state DC currents, respectively; R_0 and R_s are the charge transfer resistance values of the cell before and after DC polarization, respectively; and ΔV is the applied voltage (10 mV). The galvanostatic charge/discharge cycling tests were performed at a current density of 1 mA cm⁻². The C-rate test was conducted with a charging rate of 0.2 C and discharging rates of 0.2 ~ 10 C within a potential range of 3 ~ 4.2 V. The cycling tests were run with charging/discharging rates of 0.5 C. The AC impedance spectra of the electrolytes were evaluated over the frequency range 10⁻² Hz and 10⁶ Hz (ZIVE MP, ZIVELAB). The electrochemical stability windows of the electrolytes were evaluated via linear sweep voltammetry (LSV) at a scan rate of 1 mV s⁻¹ using an asymmetric cell Li||SUS cells.

3. Results and discussion

3.1. Semi-solid electrolytes with molecular traps

The synthesis process of the morphology-controlled MOFs is shown in Fig. 1a. A series of CAU-17 MOFs with sheet and rod morphologies were synthesized by adjusting the stirring time (Fig. 1b), and both MOFs were collected as white powders (Fig. S1). The characteristics of the morphology-controlled MOFs are shown in Fig. S2. To identify the possible reasons of the variation of morphology in methanol, the SEM image of sediments was exhibited in Fig. S3. The morphology of the sediment formed by the rapid nucleation of the CAU-17 precursor in methanol also shows a plate-like structure. This morphology suggests that the axial growth of the resulting sample was constrained by the rapid nucleation process. At the same time, radial growth was promoted during the subsequent hydrothermal process. Therefore, the preferred growth direction for the CAU-17 sheet is radial, whereas for the CAU-17 rod it is axial.

The MOF-incorporated SPEs were prepared by adding CAU-17 sheets and CAU-17 rods (denoted as S-SPE and R-SPE, respectively) to a precursor solution followed by a simple UV-curing method (Fig. S4). UV-curing method is one of the facile and effective way to enhance the mechanical strength of SPEs while maintaining their ionic conductivity [11,12]. In addition to S-SPE and R-SPE, pristine SPE without MOF was selected as the control system, denoted as c-SPE. The precursor solutions with MOFs exhibited a more translucent color than the precursor solution without MOFs, as shown in Fig. S5. After curing, a free-standing film was obtained, demonstrating the mechanical feasibility of the R-SPE (Fig. 1c). In addition, the synergistic effect of the semi-IPN polymer structure and MOFs for flame retardancy was observed in the lighting test (Fig. 1d) [43]. Upon exposure to fire for 5 s, the flames on the R-SPE self-extinguished, demonstrating the enhanced safety characteristics of the R-SPE. The role of MOFs in capturing LEs was further demonstrated by TGA in the range of 30 to 600 °C (Fig. S6). Given the boiling points of DEC (125 °C) and EC (244 °C), the plateau observed in the TGA curve at 300 °C corresponds to loss of liquid content (approximately 80 wt.%) in the SPEs. The weight loss of the R-SPE was lower than that of the SPE up to 200 °C, indicating that the solvents captured in the pore of the CAU-17 rods were less sensitive to external thermal stress. The liquid capture capability and confinement effect of MOFs were further elucidated through TGA of vacuum-dried SPEs (Fig. S7). TGA profile of the vacuum-

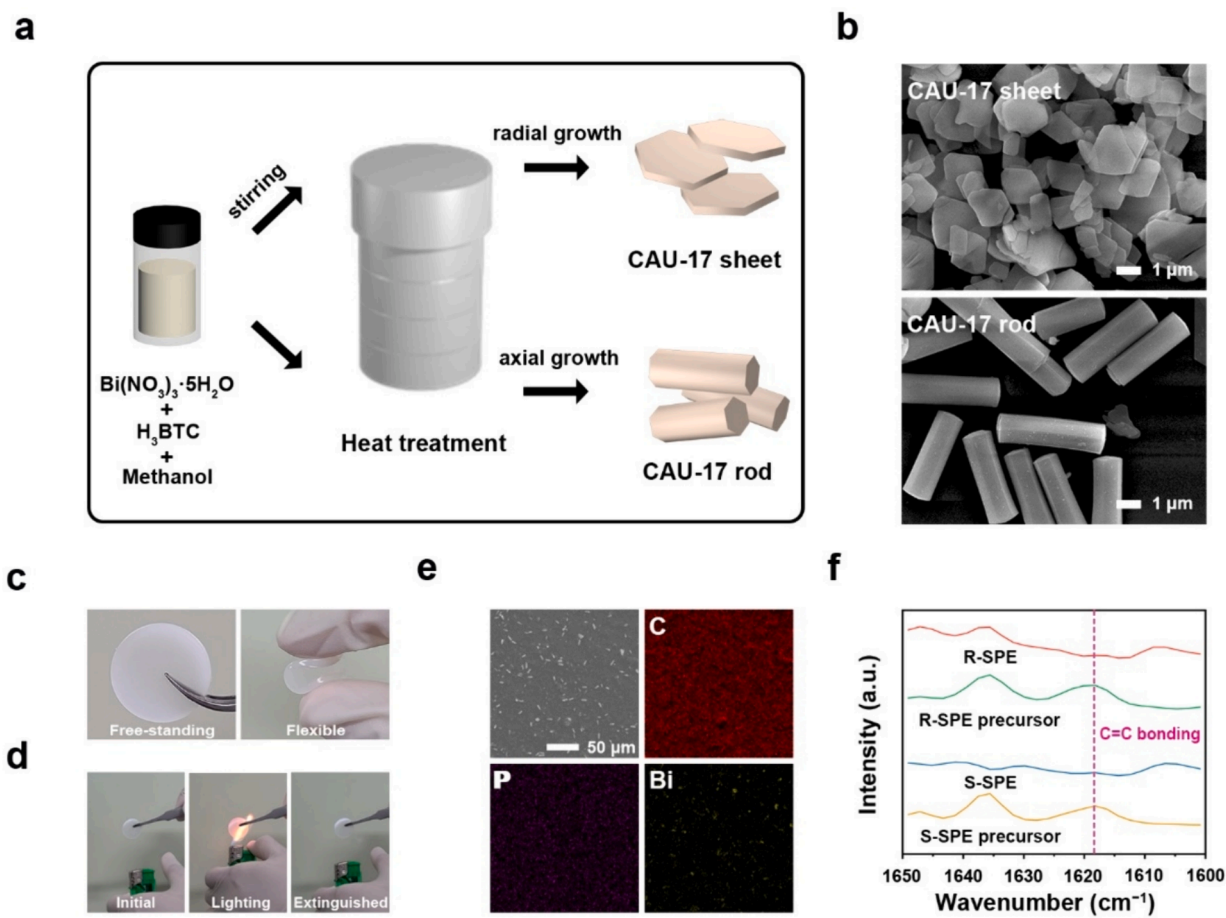


Fig. 1. Physicochemical properties of the MOF-incorporated SPEs and characterization. (a) Schematic illustration of the preparation of the morphology-controlled MOFs. (b) FE-SEM images of the CAU-17 sheets and rods. (c) Optical images and (d) fire extinguishing test of R-SPE. (e) FE-SEM and EDS images of the R-SPE. (f) FT-IR spectra of S-SPE and R-SPE before and after UV curing.

dried R-SPE demonstrated a higher liquid content compared to the vacuum-dried c-SPE, indicating that the liquid electrolyte retained by the MOFs exhibits resistance to the thermal stress encountered during the vacuum drying process.

The uniform dispersion of the MOF particles was detected and further supported by EDS, which originated from the ETPTA/PVdF-HFP polymer matrix (for C, carbon), LiPF₆ (for P, phosphorus), and MOFs (for Bi, bismuth), as shown in Fig. 1e. The completion of cross-linking was confirmed by FT-IR spectroscopy (Fig. 1f). The stretching vibrations for acrylic C=C bonds (1610–1625 cm⁻¹) disappeared after UV curing of both S-SPE and R-SPE, indicating that the ETPTA monomers were successfully cross-linked even after the addition of the MOFs. The XRD diffraction peaks corresponding to the CAU-17 disappeared from the diffraction patterns for both S-SPE and R-SPE, indicating uniform dispersion of the MOF particles in the polymer matrix (Fig. S8) [44].

3.2. Accelerating Li⁺ transport in semi-solid electrolytes

Ionic conductivities were measured to assess the enhancement of Li⁺ transport in the SPEs. The ionic conductivities were found to be directly related to the CAU-17 rod content, peaking at 1.53 mS cm⁻¹ with 3 wt.% of these rods, as shown in the impedance plot (Fig. S9). The R-SPE with this optimal 3 wt.% CAU-17 rod composition exhibited a well-distributed pattern of MOF particles (Fig. S10). The S-SPE showed slightly higher ionic conductivity than the c-SPE, and the R-SPE showed the highest value (Fig. 2a). The enhanced ionic conductivity of MOF-incorporated SPEs can be attributed to the decreased *T_g* value in DSC, where the S-SPE and R-SPE showed lower *T_g* values than the c-SPE

(Fig. 2b). Moreover, the R-SPE showed a lower *T_g* value than the S-SPE due to the greater specific surface area and aspect ratio of CAU-17 rods compared to the CAU-17 sheet. The accelerated Li⁺ conduction in the R-SPE is further enhanced by tuning electrostatic interaction (freely movable anions in liquid electrolytes and open metal sites in MOFs). As a result, the R-SPE provides higher Li⁺ conductivity (namely, ion conductivity multiplied by Li⁺ transference number) for ion conduction compared to those of c-SPE and S-SPE.

The Li⁺ transference number was measured by the Bruce-Vincent method, as shown in Fig. S11 [45]. The calculation details are summarized in Table S1. The c-SPE showed a Li⁺ transference number of 0.29, which was higher than that of the LEs, as the PVdF-HFP chains immobilized anions via ion-dipole interactions [46]. The MOF-based SPE showed a higher value as the MOFs further hindered anion transport through Lewis acid-base interactions [47]. Since the OMSs in the CAU-17 exhibited Lewis acid properties, anions were immobilized by uncoordinated Bi metals via Lewis acid-base interactions. These interactions restricted anion transport and interfered with the interactions between Li⁺ and PF₆⁻. Since the CAU-17 rods had higher surface areas than the CAU-17 sheets, the Li⁺ boosting effect was greater for the R-SPE, and the R-SPE showed the highest transference number of 0.76, demonstrating a selective Li⁺ transport capability.

The interactions between OMS and anions were analyzed by FT-IR (Fig. 2c). The PF₆⁻ peak at 840 cm⁻¹, which was originally absent in the MOF spectra, was found in the MOF/LE spectrum, indicating the incorporation of LEs into the MOF pores. Additionally, a new peak at 858 cm⁻¹ appeared in the MOF/LE spectrum, corresponding to a blue shifted peak for PF₆⁻ due to interactions with OMSs in the MOFs. This can

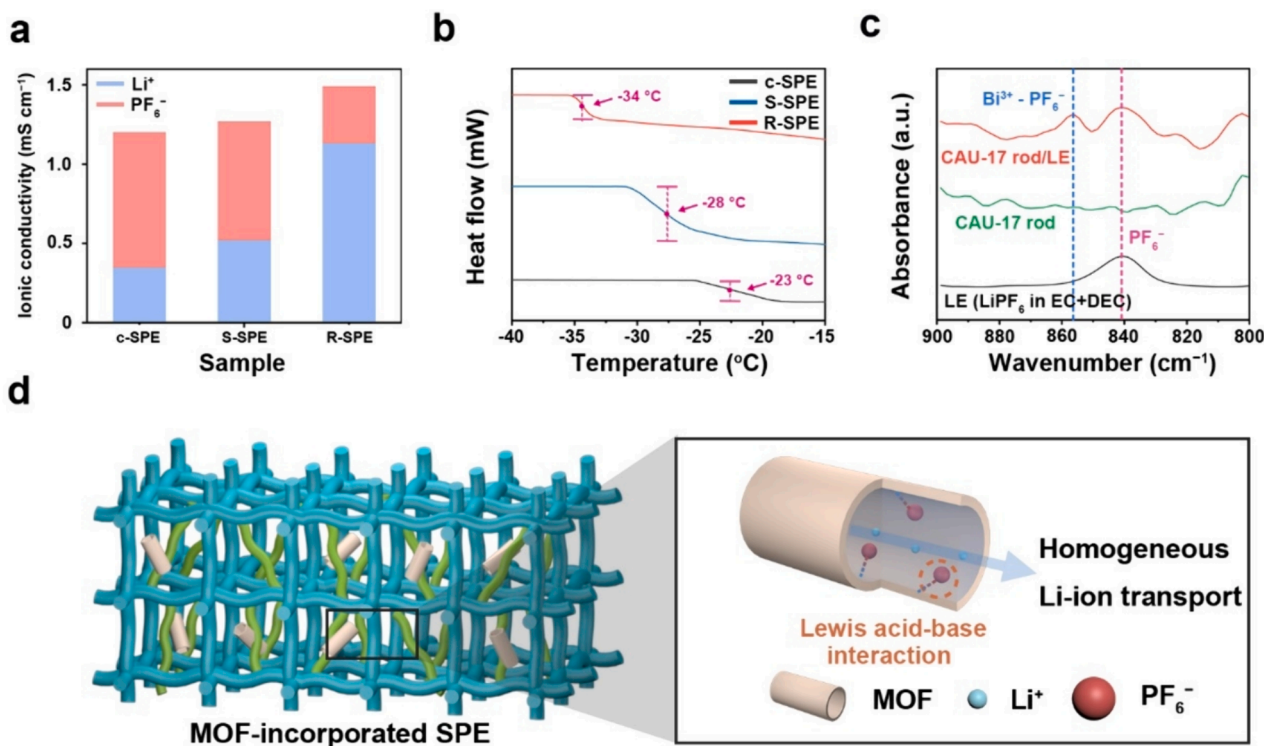


Fig. 2. Li⁺ conductivity enhancement by incorporation of MOF molecular traps. (a) Li⁺ conductivity of the R-SPE (vs. c-SPE and S-SPE) (b) DSC thermograms of the R-SPE (vs. c-SPE and S-SPE). (c) FT-IR spectra of LE, CAU-17 rods, and CAU-17 rods/LE. (d) Schematic illustration of the homogeneous Li⁺ transport mechanism through the MOFs.

also be seen in the FT-IR spectrum of the S-SPE (Fig. S12). XPS analysis was conducted to confirm the interactions between the OMSs and the anions. (Fig. S13). The aforementioned selective Li⁺ transport mechanism is schematically shown in Fig. 2d.

3.3. Theoretical analysis of lithium-ion boosting molecular traps

The MD simulations were performed to further investigate the Li⁺ transport inside the CAU-17 rod pore. The configuration of the R-SPE

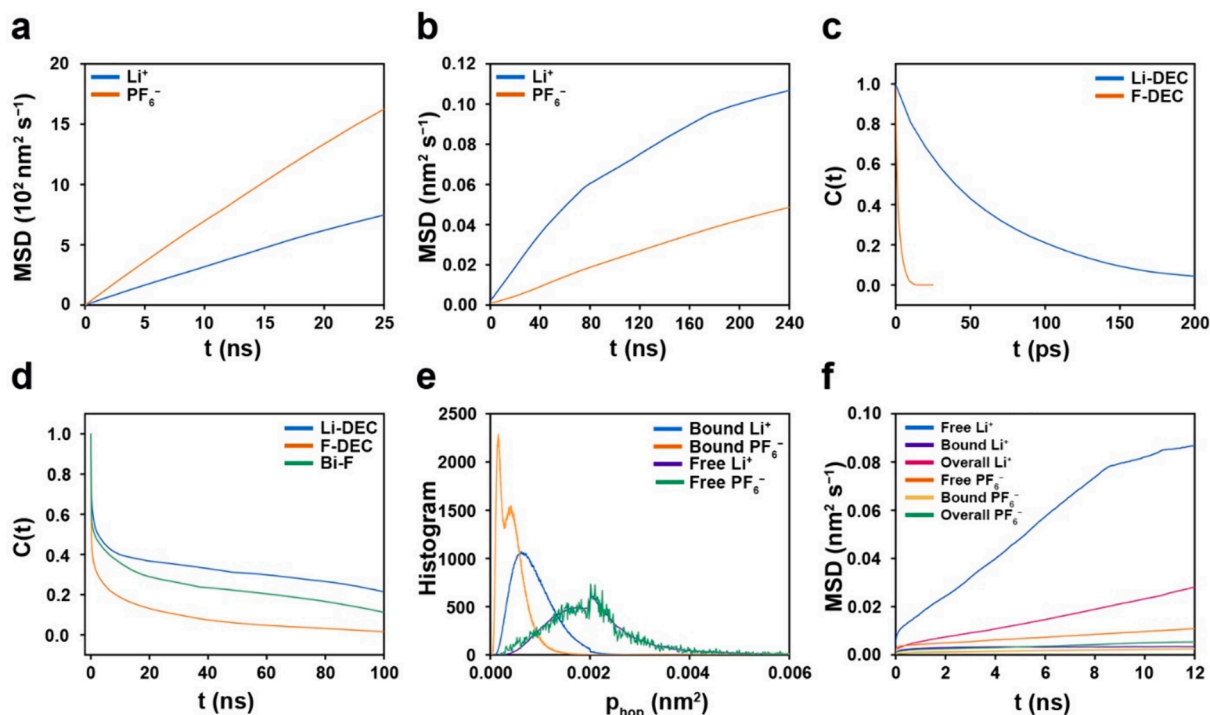


Fig. 3. Li⁺ transport mechanism in the MOF pore analyzed by MD simulations. (a) MSDs in the bulk, (b) MSDs in the CAU-17 rod pore, (c) ACFs in the bulk, (d) ACFs in the CAU-17 rod pore, (e) histogram of P_{hop} in the free and bound states for Li⁺ and PF₆⁻, and (f) MSDs in the free and bound states for Li⁺ and PF₆⁻.

used in the MD simulations is shown in Fig. S14. The bulk MSDs showed that PF_6^- diffused faster than Li^+ (Fig. 3a). However, inside the CAU-17 rod pore, the opposite was true; the Li^+ diffused faster than the PF_6^- (Fig. 3b). To investigate the difference, the diffusion of ions was further analyzed, considering that the diffusion of ions is hindered by the local structure formation. Their contribution is studied by examining the radial distribution functions (RDFs) of an ion (Fig. S15) from its neighboring molecules and their auto-correlation function (ACF). In the bulk, the 'Li-DEC' pair lasts much longer than any other pair (Fig. 3c), meaning that the Li^+ are bound to the DEC. Li^+ and DEC diffuse in their solvation shell as a single entity, known as vehicular diffusion. The larger effective mass of the Li^+ and DEC complex retards the Li^+ diffusion. In contrast, PF_6^- are not bound to the solvents and can diffuse freely. In the pore, PF_6^- is strongly bound to immobile Bi atoms, which significantly slows down the PF_6^- diffusion (Fig. 3d).

To detect the hopping motion of caged or bound ions, two states are classified using a quantity called P_{hop} (Fig. S16), following the classification outlined in the previous works [48,49]. The classified P_{hop} s are shown in Fig. S17. The average P_{hop} of Li^+ is higher than that of PF_6^- , as expected. Fig. 3e shows the normalized histograms of P_{hop} . The histograms are narrower in the bound state, indicating that the ions fluctuate only in a limited range. The free state ions have a broader histogram, indicating that the ions are diffusing around. We can infer that free state ions diffuse faster than bound state ions and contribute more to the total diffusion, and the free state fraction is key to understanding the delayed diffusion in the pore. Li^+ remains in the free state for about 12% of the time, while PF_6^- remains in the free state only 1% of the time. The total diffusion is a weighted sum of the two states. Fig. 3f confirms that the free state ions contribute dominantly to the diffusion. We provided probability distribution functions (PDFs) of dr for each state, and dr in the free states has a broader distribution, larger than dr in the bound state (Fig. S17c). In the free state, both Li^+ and PF_6^- can have larger values of dr , indicating favorable ion diffusion in the pore than in the bound state, but Li^+ is more likely to diffuse as the fraction of Li^+ in the free state is larger than that of PF_6^- . As PF_6^- are coordinated to the OMS of the MOF, only free Li^+ contribute to the conductivity. Thus, the high Li^+ transference number of R-SPE originates from the selective Li^+ transport mechanisms in the CAU-17 rod pore (Supplementary Video 1).

3.4. Practical semi-solid lithium metal batteries

The electrochemical stability of the SPEs was analyzed using LSV. The S-SPE and R-SPE exhibited wider electrochemical stability windows than the c-SPE, indicating the high stability of the CAU-17 against oxidation (Fig. S18a). Li deposition was tested with the $\text{Li}||\text{Cu}$ cells, and the cells with R-SPE exhibited much lower nucleation overpotentials and plateau overpotentials than c-SPE, demonstrating superior electrochemical kinetics for Li plating in the R-SPE systems (Fig. S19). The morphology of the plated Li was analyzed by FE-SEM. The Li plated with the c-SPE showed non-uniform, dendritic Li growth, while the Li plated with the MOF-based SPEs showed uniform and smooth morphologies, indicating stable Li plating behavior (Fig. S20). The R-SPE exhibited the highest cycling stability, remaining short-circuit free for up to 300 h in the galvanostatic cycling test, due to the highest Li^+ conductivity, which facilitated uniform Li deposition (Fig. S18b). The enhanced Li plating/stripping kinetics observed in the R-SPE can be attributed to the electrostatic interactions between the MOFs and anions, which act as Li^+ boosting molecular traps due to the anion immobilization. According to Chazalviel's sand time theory, the suppression of the concentration gradient caused by anions effectively reduces the effective current density, thus promoting dendrite-free Li plating [50]. The dendrite suppression capability of the R-SPE is shown schematically in Fig. S18c.

To explore the potential applications of the R-SPE to SSLMBs at room temperature, we investigated the effect of the Li^+ boosting MOF molecular traps on the electrochemical performance. To mitigate the risk of short-circuiting during high C-rate charge/discharge cycles, a PE

membrane was integrated to ensure stable operational conditions. The charge and discharge performances of SSLMB cells with R-SPE were investigated by using a Li-metal cell (NCM712 cathode|R-SPE|Li-metal anode). The R-SPE cell exhibited higher discharge capacities than the control cells (c-SPE and S-SPE) over a wide range of discharge current densities (0.2 to 10.0 C) (Fig. 4a). Such faster rate capabilities of the R-SPE cell are consistent with the faster electrochemical reaction kinetics of the electrodes when integrated with R-SPE. The cycling performance of the cell was examined at a current density of 0.5 C and room temperature conditions (Fig. 4b and c). The R-SPE cell showed a higher capacity retention (86% after 200 cycles) compared to the control cells (c-SPE: 74% and S-SPE: 80%). This superior cyclability could be related to the selective and uniform Li^+ transport capability of the R-SPE, which formed a stable interface between the electrolyte and the electrodes without formation of the Li dendrites.

Such superior cyclability of the R-SPE cell was verified by analyzing the electrochemical impedance spectroscopy (EIS) spectra (Fig. 4d and e). This result is consistent with the superior Li plating behavior of the R-SPE confirmed by $\text{Li}||\text{Li}$ symmetric cell, as the high Li^+ transference number of the R-SPE could reduce the concentration polarization and promote the stable SEI layer formation. A comparison with previously reported MOF-based SPEs showed that the R-SPE SSLMB cell exhibited exceptional discharge capacity even at high C-rate of 10 C, which has never been reported in the previous studies of SSLMBs (Fig. S21). Due to the superior Li^+ transport mechanism, the pouch-type R-SPE cell achieved reliable cycling performance with stable capacity retention (86.7% after 100 cycles), indicating the reliability of R-SPE in practical applications (Fig. 4f). Considering the possibility of application to the stacked cells, R-SPE can explore the application of solid-state electrolyte in a practical energy source with high energy density [12]. Comparison with previously reported porous materials incorporating SPE confirms the superior performance of R-SPE, which far exceeds those reported in previous studies on SSLMBs with porous crystalline framework (Fig. 4g) [51–56].

The surfaces of the Li-metal anode were observed after 100 cycles to investigate the interfacial properties. The image of the Li-metal surface with the c-SPE showed more porosity and more extensive dendritic Li growth compared to the bare Li-metal (Fig. 5a). In contrast, the surface of the Li-metal with the R-SPE showed a relatively smooth and dense SEI layer, demonstrating the effectiveness of the R-SPE in suppressing dendrite growth. Structural changes in the cycled Li metal were further elucidated by conducting XPS analysis. The C1s spectra showed the presence of Li_2CO_3 , which form via the decomposition of carbonate-based solvents [57], on the top of the Li-metals for both the R-SPE and c-SPE. This indicates that carbonate solvents act as a charge carrier medium in the R-SPE as well as the c-SPE (Fig. S22). Since PF_6^- was immobilized on the OMSs of the MOF in the R-SPE, the F1s spectra of the R-SPE had weaker characteristic peaks corresponding to LiF and $\text{Li}_x\text{P-F}_y\text{O}_z$ species, which stemmed from the decomposition of LiPF_6 , compared to those of the liquid electrolyte. Notably, a high ratio of LiF to $\text{Li}_x\text{P-F}_y\text{O}_z$ (as a side reactive by-product) was formed compared to c-SPE, which is beneficial in forming a stable and robust SEI layer that retards Li dendrite growth. (Fig. 5b and c) [57,58]. This XPS characterization is consistent with the ion conduction and electrostatic interactions in R-SPE, underscoring the advantages of the R-SPE as a Li^+ boosting molecular traps in stabilizing the surface of Li-metal anodes.

4. Conclusions

In summary, systematic designs were conducted to analyze the relationship between morphology and Li^+ transport behavior in MOF-based SPEs using two types of bismuth MOFs, CAU-17 sheets and CAU-17 rods. CAU-17 rods with high specific area and high aspect ratio interacted with the polymer matrix and Li salts to generate free Li^+ , thereby exhibiting high Li^+ conductivity ($\sigma = 1.53 \text{ mS cm}^{-1}$, $t_{\text{Li}^+} = 0.76$) for R-SPE. The OMSs in the MOFs interacted with PF_6^- in the electrolyte

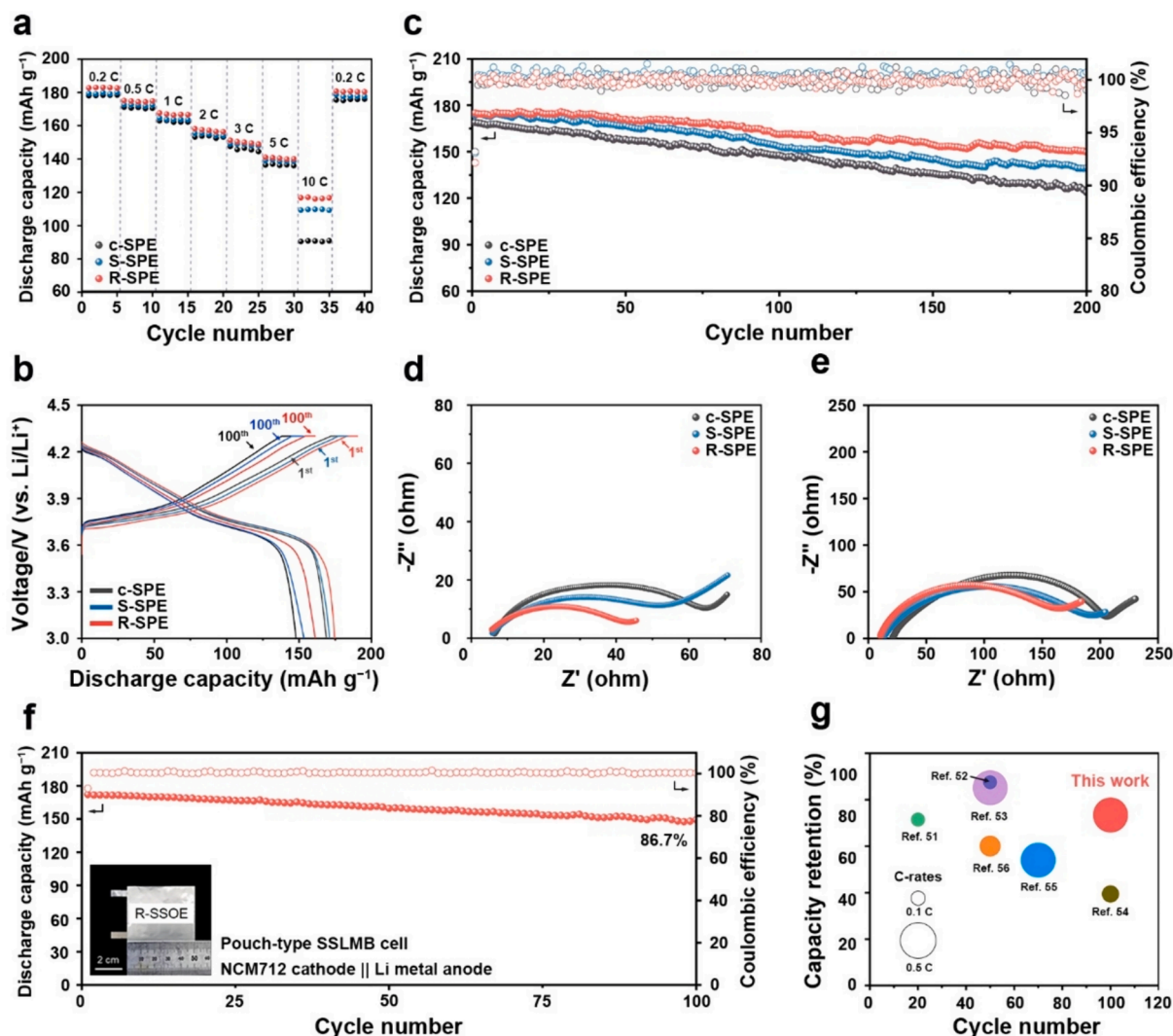


Fig. 4. Electrochemical performance of the SSLMB at room temperature. (a) Rate capability of the cells (NCM712cathode|R-SPE (vs. c-SPE and S-SPE)|Li-metal anode), in which the discharge current densities were varied from 0.2 to 10.0 C at a fixed charge current density of 0.2 C. (b) Voltage profiles and (c) cycling performance of the R-SPE cells versus the control cells with c-SPE and S-SPE at a current density of 0.5 C. EIS profiles of R-SPE cells after the cycling test: (d) 1st cycle and (e) 100th cycle. (f) Cycling performance of the pouch-type R-SPE cell at a current density of 0.5 C. The inset shows the optical image. (g) Comparison of the R-SPE cell (this study) vs. previously reported cells with porous crystalline materials in terms of three parameters: cycle number (x-axis), capacity retention (y-axis), C-rate (diameter).

to provide a homogeneous Li^+ transport channel, as elucidated by MD simulations and calculations. The R-SPE cell exhibited superior interfacial properties, resulting in high discharge capacity (182 mAh g^{-1} at 0.2 C and 116 mAh g^{-1} at 10 C) and stable cycling performance (86% after 200 cycles), which demonstrated stable dendrite-free Li deposition behavior. In addition, a pouch-type SSLMB cell using R-SPE was fabricated and tested to demonstrate the reliability of R-SPE in practical applications. This work presents a new class of molecular trap designed by controlling the morphology of MOFs to accelerate Li^+ transport. A comprehensive study was conducted to understand the relationship between MOF morphology and the Li^+ transport in SPE-based SSLMB, suggesting that systematic investigation of the MOF morphology would further improve the performance of MOF-incorporated SPE.

Author contributions

J. H. Park designed the experimental process. D. Lee and K-S. Oh carried out the materials synthesis, characterization and wrote the paper. J. Jin carried out the materials synthesis. Y. Lee and Y. Jho conducted MD simulations. S-Y. Lee helped discussed the experimental

results and modify the manuscript.

CRediT authorship contribution statement

Daero Lee: Writing – review & editing, Writing – original draft, Formal analysis, Data curation. **Kyeong-Seok Oh:** Writing – review & editing, Writing – original draft, Formal analysis, Data curation. **Yeongkyu Lee:** Writing – original draft, Data curation. **Jie Jin:** Writing – original draft, Formal analysis, Data curation. **Sang-Young Lee:** Writing – review & editing, Writing – original draft, Data curation, Conceptualization. **Yongseok Jho:** Writing – original draft, Data curation. **Jong Hyeok Park:** Writing – review & editing, Writing – original draft, Data curation, Conceptualization.

Declaration of competing interest

The authors declare that they have no known competing financial interests or personal relationships that could have appeared to influence the work reported in this paper.

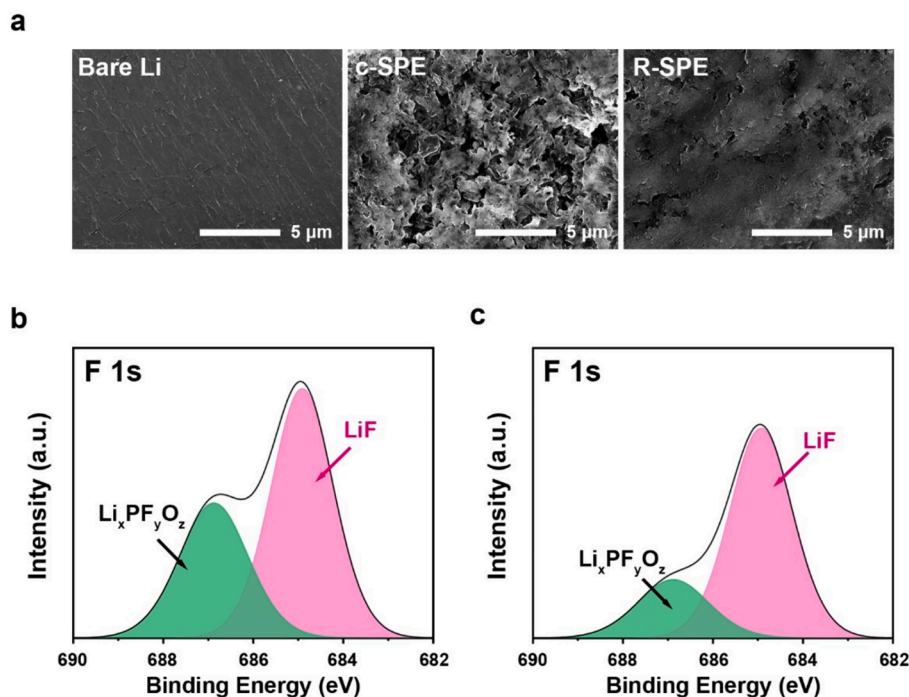


Fig. 5. Post-mortem analysis of Li-metal anode. (a) SEM images (surface) of the cycled Li-metal anodes (after 100 cycles): (left) bare Li, (middle) c-SPE, (right) R-SPE. F1s XPS analysis of the cycled Li-metal anodes with (b) the c-SPE and (c) the R-SPE.

Data availability

Data will be made available on request.

Acknowledgements

This work was supported by grants from National Research Foundation of Korea (NRF) grants funded by the Korea Government (MSIT) (2022M3J1A1054151, 2022M3J1A1085397, RS-2023-00302697).

Appendix A. Supplementary data

Supplementary data to this article can be found online at <https://doi.org/10.1016/j.cej.2024.153825>.

References

- [1] C. Niu, D. Liu, J.A. Lochala, C.S. Anderson, X. Cao, M.E. Gross, W. Xu, J.G. Zhang, M.S. Whittingham, J. Xiao, J. Liu, Balancing interfacial reactions to achieve long cycle life in high-energy lithium metal batteries, *Nat. Energy* 6 (2021) 723–732, <https://doi.org/10.1038/s41560-021-00852-3>.
- [2] K.J. Jun, Y. Sun, Y. Xiao, Y. Zeng, R. Kim, H. Kim, L.J. Miara, D. Im, Y. Wang, G. Ceder, Lithium superionic conductors with corner-sharing frameworks, *Nat. Mater.* 21 (2022) 924–931, <https://doi.org/10.1038/s41563-022-01222-4>.
- [3] M.S. Kim, Z. Zhang, P.E. Rudnicki, Z. Yu, J. Wang, H. Wang, S.T. Oyakhire, Y. Chen, S.C. Kim, W. Zhang, D.T. Boyle, X. Kong, R. Xu, Z. Huang, W. Huang, S. F. Bent, L.W. Wang, J. Qin, Z. Bao, Y. Cui, Suspension electrolyte with modified Li⁺ solvation environment for lithium metal batteries, *Nat. Mater.* 21 (2022) 445–454, <https://doi.org/10.1038/s41563-021-01172-3>.
- [4] L. Qiao, U. Oteo, M. Martinez-Ibanez, A. Santiago, R. Cid, E. Sanchez-Diez, E. Lobato, L. Meabe, M. Armand, H. Zhang, Stable non-corrosive sulfonimide salt for 4-V-class lithium metal batteries, *Nat. Mater.* 21 (2022) 455–462, <https://doi.org/10.1038/s41563-021-01190-1>.
- [5] S. Li, J. Huang, Y. Cui, S. Liu, Z. Chen, W. Huang, C. Li, R. Liu, R. Fu, D. Wu, A robust all-organic protective layer towards ultrahigh-rate and large-capacity Li metal anodes, *Nat. Nanotechnol.* 17 (2022) 613–621, <https://doi.org/10.1038/s41565-022-01107-2>.
- [6] H. Chen, Y. Yang, D.T. Boyle, Y.K. Jeong, R. Xu, L.S. de Vasconcelos, Z. Huang, H. Wang, H. Wang, W. Huang, H. Li, J. Wang, H. Gu, R. Matsumoto, K. Motohashi, Y. Nakayama, K. Zhao, Y. Cui, Free-standing ultrathin lithium metal–graphene oxide host foils with controllable thickness for lithium batteries, *Nat. Energy* 6 (2021) 790–798, <https://doi.org/10.1038/s41560-021-00833-6>.
- [7] M.J. Lee, J. Han, K. Lee, Y.J. Lee, B.G. Kim, K.N. Jung, B.J. Kim, S.W. Lee, Elastomeric electrolytes for high-energy solid-state lithium batteries, *Nature* 601 (2022) 217–222, <https://doi.org/10.1038/s41586-021-04209-4>.
- [8] T. Wang, J. Duan, B. Zhang, W. Luo, X. Ji, H. Xu, Y. Huang, L. Huang, Z. Song, J. Wen, C. Wang, Y. Huang, J.B. Goodenough, A self-regulated gradient interphase for dendrite-free solid-state Li batteries, *Energy Environ. Sci.* 15 (2022) 1325–1333, <https://doi.org/10.1039/d1ee03604a>.
- [9] A. Hu, W. Chen, X. Du, Y. Hu, T. Lei, H. Wang, L. Xue, Y. Li, H. Sun, Y. Yan, J. Long, C. Shu, J. Zhu, B. Li, X. Wang, J. Xiong, An artificial hybrid interphase for an ultrahigh-rate and practical lithium metal anode, *Energy Environ. Sci.* 14 (2021) 4115–4124, <https://doi.org/10.1039/d1ee00508a>.
- [10] S. Huo, L. Sheng, W. Xue, L. Wang, H. Xu, H. Zhang, X. He, Challenges of polymer electrolyte with wide electrochemical window for high energy solid-state lithium batteries, *InfoMat* 5 (2023) 12394, <https://doi.org/10.1002/inf2.12394>.
- [11] Y.G. Choi, J.C. Shin, A. Park, Y.M. Jeon, J. Il Kim, S. Kim, S. Kim, W.B. Lee, M. Lee, J.H. Park, Pyrrolidinium-PEG Ionic Copolyester: Li-Ion Accelerator in Polymer Network Solid-State Electrolytes, *Adv. Energy Mater.* 11 (2021) 2102660, <https://doi.org/10.1002/aenm.202102660>.
- [12] K.S. Oh, J.H. Kim, S.H. Kim, D. Oh, S.P. Han, K. Jung, Z. Wang, L. Shi, Y. Su, T. Yim, S. Yuan, S.Y. Lee, Single-Ion Conducting Soft Electrolytes for Semi-Solid Lithium Metal Batteries Enabling Cell Fabrication and Operation under Ambient Conditions, *Adv. Energy Mater.* 11 (2021) 2101813, <https://doi.org/10.1002/aenm.202101813>.
- [13] S. Huang, Y.P. Huang, Y. Xia, J. Ding, C. Peng, L. Wang, J. Luo, X.X. Zhang, J. Zheng, Y.Q. Gao, J. Chen, High Li⁺ coordinated solvation sheaths enable high-quality Li metal anode, *InfoMat* 5 (2023) 12411, <https://doi.org/10.1002/inf2.12411>.
- [14] M. Balaish, J.C. Gonzalez-Rosillo, K.J. Kim, Y. Zhu, Z.D. Hood, J.L.M. Rupp, Processing thin but robust electrolytes for solid-state batteries, *Nat. Energy* 6 (2021) 227–239, <https://doi.org/10.1038/s41560-020-00759-5>.
- [15] Y.T. Xu, S.J. Dai, X.F. Wang, X.W. Wu, Y.G. Guo, X.X. Zeng, An ion-percolating electrolyte membrane for ultrahigh efficient and dendrite-free lithium metal batteries, *InfoMat* 5 (2023) 12498, <https://doi.org/10.1002/inf2.12498>.
- [16] Y. Liu, X. Meng, Z. Wang, J. Qiu, Development of quasi-solid-state anode-free high-energy lithium sulfide-based batteries, *Nat. Commun.* 13 (2022) 4415, <https://doi.org/10.1038/s41467-022-32031-7>.
- [17] J. Wan, J. Xie, X. Kong, Z. Liu, K. Liu, F. Shi, A. Pei, H. Chen, W. Chen, J. Chen, X. Zhang, L. Zong, J. Wang, L.Q. Chen, J. Qin, Y. Cui, Ultrathin, flexible, solid polymer composite electrolyte enabled with aligned nanoporous host for lithium batteries, *Nat. Nanotechnol.* 14 (2019) 705–711, <https://doi.org/10.1038/s41565-019-0465-3>.
- [18] A. Hu, Z. Liao, J. Huang, Y. Zhang, Q. Yang, Z. Zhang, L. Yang, S. ichi Hirano, In-situ construction of dual lithium-ion migration channels in polymer electrolytes for lithium metal batteries, *Chem. Eng. J.* 448 (2022) 137661, <https://doi.org/10.1016/j.cej.2022.137661>.
- [19] J. Pan, P. Zhao, N. Wang, F. Huang, S. Dou, Research progress in stable interfacial constructions between composite polymer electrolytes and electrodes, *Energy Environ. Sci.* 15 (2022) 2753–2775, <https://doi.org/10.1039/d1ee03466a>.

- [20] K. Lu, H. Ruan, S. Meng, Q. Zhao, J. Ji, Y. Wu, C. Wang, S. Tan, Smectic solid electrolytes containing lamellar conducting channels for solvent-free lithium-ion batteries with a thermal switch on/off performance, *Chem. Eng. J.* 475 (2023) 146418, <https://doi.org/10.1016/j.cej.2023.146418>.
- [21] X. Zhang, J. Xie, F. Shi, D. Lin, Y. Liu, W. Liu, A. Pei, Y. Gong, H. Wang, K. Liu, Y. Xiang, Y. Cui, Vertically Aligned and Continuous Nanoscale Ceramic-Polymer Interfaces in Composite Solid Polymer Electrolytes for Enhanced Ionic Conductivity, *Nano Lett.* 18 (2018) 3829–3838, <https://doi.org/10.1021/acs.nanolett.8b01111>.
- [22] D. Zhou, R. Liu, Y.B. He, F. Li, M. Liu, B. Li, Q.H. Yang, Q. Cai, F. Kang, SiO₂ Hollow Nanosphere-Based Composite Solid Electrolyte for Lithium Metal Batteries to Suppress Lithium Dendrite Growth and Enhance Cycle Life, *Adv. Energy Mater.* 6 (2016) 1502214, <https://doi.org/10.1002/aenm.201502214>.
- [23] F. Wu, N. Chen, R. Chen, Q. Zhu, G. Tan, L. Li, Self-regulative nanogelator solid electrolyte: A new option to improve the safety of lithium battery, *Adv. Sci.* 3 (2015) 1–9, <https://doi.org/10.1002/adv.201500306>.
- [24] J. Yin, X. Xu, S. Jiang, H. Wu, L. Wei, Y. Li, J. He, K. Xi, Y. Gao, High ionic conductivity PEO-based electrolyte with 3D framework for Dendrite-free solid-state lithium metal batteries at ambient temperature, *Chem. Eng. J.* 431 (2022) 133352, <https://doi.org/10.1016/j.cej.2021.133352>.
- [25] S. Zheng, Y. Chen, K. Chen, S. Yang, R. Bagherzadeh, Y.E. Miao, T. Liu, In situ construction of polyether-based composite electrolyte with bi-phase ion conductivity and stable electrolyte/electrode interphase for solid-state lithium metal batteries, *J. Mater. Chem. A* 10 (2022) 19641–19648, <https://doi.org/10.1039/d2ta02229j>.
- [26] R. Zhao, Y. Wu, Z. Liang, L. Gao, W. Xia, Y. Zhao, R. Zou, Metal-organic frameworks for solid-state electrolytes, *Energy Environ. Sci.* 13 (2020) 2386–2403, <https://doi.org/10.1039/d0ee00153h>.
- [27] Q. Zhang, B. Liu, J. Wang, Q. Li, D. Li, S. Guo, Y. Xiao, Q. Zeng, W. He, M. Zheng, Y. Ma, S. Huang, The optimized interfacial compatibility of metal-organic frameworks enables a high-performance quasi-solid metal battery, *ACS Energy Lett.* 5 (2020) 2919–2926, <https://doi.org/10.1021/acseenergylett.0c01517>.
- [28] H. Hong, J. Liu, H. Huang, C. Atangana Etoyo, X. Yang, B. Guan, L. Zhang, Ordered Macro-Microporous Metal-Organic Framework Single Crystals and Their Derivatives for Rechargeable Aluminum-Ion Batteries, *J. Am. Chem. Soc.* 141 (2019) 14764–14771, <https://doi.org/10.1021/jacs.9b06957>.
- [29] L. Du, B. Zhang, W. Deng, Y. Cheng, L. Xu, L. Mai, Hierarchically Self-Assembled MOF Network Enables Continuous Ion Transport and High Mechanical Strength, *Adv. Energy Mater.* 12 (2022) 2200501, <https://doi.org/10.1002/aenm.202200501>.
- [30] Z. Chang, H. Yang, X. Zhu, P. He, H. Zhou, A stable quasi-solid electrolyte improves the safe operation of highly efficient lithium-metal pouch cells in harsh environments, *Nat Commun.* 13 (2022) 1510, <https://doi.org/10.1038/s41467-022-29118-6>.
- [31] W.L. Xue, W.H. Deng, H. Chen, R.H. Liu, J.M. Taylor, Y. kun Li, L. Wang, Y. H. Deng, W.H. Li, Y.Y. Wen, G.E. Wang, C.Q. Wan, G. Xu, MOF-Directed Synthesis of Crystalline Ionic Liquids with Enhanced Proton Conduction, *Angew. Chem. – Int. Ed.* 60 (2021) 1290–1297, <https://doi.org/10.1002/anie.202010783>.
- [32] L. Shen, H. Bin Wu, F. Liu, J.L. Brosmer, G. Shen, X. Wang, J.I. Zink, Q. Xiao, M. Cai, G. Wang, Y. Lu, B. Dunn, Creating Lithium-Ion Electrolytes with Biomimetic Ionic Channels in Metal-Organic Frameworks, *Adv. Mater.* 30 (2018) 1707476, <https://doi.org/10.1002/adma.201707476>.
- [33] M. Zhang, P. Pan, Z. Cheng, J. Mao, L. Jiang, C. Ni, S. Park, K. Deng, Y. Hu, K.K. Fu, Flexible, Mechanically Robust, Solid-State Electrolyte Membrane with Conducting Oxide-Enhanced 3D Nanofiber Networks for Lithium Batteries, *Nano Lett.* 21 (2021) 7070–7078, <https://doi.org/10.1021/acs.nanolett.1c01704>.
- [34] H. Ouyang, N. Chen, G. Chang, X. Zhao, Y. Sun, S. Chen, H. Zhang, D. Yang, Selective Capture of Toxic Selenite Anions by Bismuth-based Metal-Organic Frameworks, *Angew. Chem. Int. Ed.* 57 (2018) 13197–13201, <https://doi.org/10.1002/anie.201807891>.
- [35] A.K. Inge, M. Köppen, J. Su, M. Feyand, H. Xu, X. Zou, M. O’Keeffe, N. Stock, Unprecedented Topological Complexity in a Metal-Organic Framework Constructed from Simple Building Units, *J. Am. Chem. Soc.* 138 (2016) 1970–1976, <https://doi.org/10.1021/jacs.5b12484>.
- [36] B. Zhou, W. Li, J. Zhang, Theoretical Simulation of CH₄ Separation from H₂ in CAU-17 Materials, *J. Phys. Chem. C* 121 (2017) 20197–20204, <https://doi.org/10.1021/acs.jpcc.7b07108>.
- [37] W.L. Jorgensen, D.S. Maxwell, J. Tirado-Rives, Development and testing of the OPLS all-atom force field on conformational energetics and properties of organic liquids, *J. Am. Chem. Soc.* 118 (1996) 11225–11236, <https://doi.org/10.1021/ja9621760>.
- [38] X. Zhong, Z. Liu, D. Cao, Improved classical united-atom force field for imidazolium-based ionic liquids: Tetrafluoroborate, hexafluorophosphate, methylsulfate, trifluoromethylsulfonate, acetate, trifluoroacetate, and bis (trifluoromethylsulfonyl)amide, *J. Phys. Chem. B* 115 (2011) 10027–10040, <https://doi.org/10.1021/jp204148q>.
- [39] L. Martínez, R. Andrade, E.G. Birgin, J.M. Martínez, Software News and Update Packmol : A Package for Building Initial Configurations, *J. Comput. Chem.* 30 (2009) 2157, <https://doi.org/10.1002/jcc>.
- [40] M. James, T. Murtola, R. Schulz, J.C. Smith, B. Hess, E. Lindahl, ScienceDirect GROMACS : High performance molecular simulations through multi-level parallelism from laptops to supercomputers, *Software X* 2 (2015) 19–25, <https://doi.org/10.1016/j.softx.2015.06.001>.
- [41] S.S. Schoenholz, E.D. Cubuk, D.M. Sussman, E. Kaxiras, A.J. Liu, A structural approach to relaxation in glassy liquids, *Nat. Phys.* 12 (2016) 469–471, <https://doi.org/10.1038/nphys3644>.
- [42] Y. Lee, Y.K. Lee, S.M. Jeong, A. Kumar, Y.S. Jho, Two Local States of Ambient Water, *J. Korean Phys. Soc.* 76 (2020) 1–7, <https://doi.org/10.3938/jkps.76.1>.
- [43] J. Liu, J. Wang, L. Zhu, X. Chen, G. Yi, Q. Ma, S. Sun, N. Wang, X. Cui, Q. Chai, J. Feng, W. Yan, In situ grown MOFs and PVDF-HFP co-modified aramid gel nanofiber separator for high-safety lithium–sulfur batteries, *J. Mater. Chem. A* 10 (2022) 14098–14110, <https://doi.org/10.1039/d2ta03301a>.
- [44] K. He, S.H.S. Cheng, J. Hu, Y. Zhang, H. Yang, Y. Liu, W. Liao, D. Chen, C. Liao, X. Cheng, Z. Lu, J. He, J. Tang, R.K.Y. Li, C. Liu, In-Situ Intermolecular Interaction in Composite Polymer Electrolyte for Ultralong Life Quasi-Solid-State Lithium Metal Batteries, *Angew. Chem. – Int. Ed.* 60 (2021) 12116–12123, <https://doi.org/10.1002/anie.202103403>.
- [45] K.-S. Oh, S. Park, J.-S. Kim, Y. Yao, J.-H. Kim, J. Guo, D.-H. Seo, S.-Y. Lee, Electrostatic Covalent Organic Frameworks as On-Demand Molecular Traps for High-Energy Li Metal Battery Electrodes, *ACS Energy Lett.* 8 (2023) 2463–2474, <https://doi.org/10.1021/acseenergylett.3c00600>.
- [46] L. Li, M. Wang, J. Wang, F. Ye, S. Wang, Y. Xu, J. Liu, G. Xu, Y. Zhang, Y. Zhang, C. Yan, N.V. Medhekar, M. Liu, Y. Zhang, Asymmetric gel polymer electrolyte with high lithium ion conductivity for dendrite-free lithium metal batteries, *J. Mater. Chem. A* 8 (2020) 8033–8040, <https://doi.org/10.1039/d0ta01883j>.
- [47] J. Yu, T. Guo, C. Wang, Z. Shen, X. Dong, S. Li, H. Zhang, Z. Lu, Engineering Two-Dimensional Metal-Organic Framework on Molecular Basis for Fast Li+ Conduction, *Nano Lett.* 21 (2021) 5805–5812, <https://doi.org/10.1021/acs.nanolett.1c01534>.
- [48] V. Bapst, T. Keck, A. Grabska-Barwińska, C. Donner, E.D. Cubuk, S.S. Schoenholz, A. Obika, A.W.R. Nelson, T. Back, D. Hassabis, P. Kohli, Unveiling the predictive power of static structure in glassy systems, *Nat Phys* 16 (2020) 448–454, <https://doi.org/10.1038/s41567-020-0842-8>.
- [49] T. Xie, A. France-Lanord, Y. Wang, Y. Shao-Horn, J.C. Grossman, Graph dynamical networks for unsupervised learning of atomic scale dynamics in materials, *Nat Commun* 10 (2019), <https://doi.org/10.1038/s41467-019-10663-6>.
- [50] J.-N. Chazalviel, Electrochemical aspects of the generation of ramified metallic electrodeposits, *Phys. Rev. A* 42 (1990) 7355–7367, <https://doi.org/10.1103/PhysRevA.42.7355>.
- [51] W. Gong, Y. Ouyang, S. Guo, Y. Xiao, Q. Zeng, D. Li, Y. Xie, Q. Zhang, S. Huang, Covalent Organic Framework with Multi-Cationic Molecular Chains for Gate Mechanism Controlled Superionic Conduction in All-Solid-State Batteries, *Angew. Chem. – Int. Ed.* 62 (2023) e202302505.
- [52] Y. Li, W. Chen, T. Lei, H. Xie, A. Hu, F. Wang, J. Huang, X. Wang, Y. Hu, C. Yang, J. Xiong, Reconstruction suppressed solid-electrolyte interphase by functionalized metal-organic framework, *Energy Storage Mater.* 59 (2023) 102765, <https://doi.org/10.1016/j.ensm.2023.04.004>.
- [53] Y. Nie, T. Yang, D. Luo, Y. Liu, Q. Ma, L. Yang, Y. Yao, R. Huang, Z. Li, E. M. Akinoglu, G. Wen, B. Ren, N. Zhu, M. Li, H. Liao, L. Tan, X. Wang, Z. Chen, Tailoring Vertically Aligned Inorganic-Polymer Nanocomposites with Abundant Lewis Acid Sites for Ultra-Stable Solid-State Lithium Metal Batteries, *Adv. Energy Mater.* 13 (2023) 2204218, <https://doi.org/10.1002/aenm.202204218>.
- [54] H. Yang, Y. Qiao, Z. Chang, P. He, H. Zhou, Designing Cation-Solvent Fully Coordinated Electrolyte for High-Energy-Density Lithium-Sulfur Full Cell Based On Solid-Solid Conversion, *Angew. Chem. – Int. Ed.* 60 (2021) 17726–17734, <https://doi.org/10.1002/anie.202106788>.
- [55] Z. Chen, W. Zhao, Q. Liu, Y. Xu, Q. Wang, J. Lin, H. Bin Wu, Janus Quasi-Solid Electrolyte Membranes with Asymmetric Porous Structure for High-Performance Lithium-Metal Batteries, *Nanomicro Lett.* 16 (2024), <https://doi.org/10.1007/s40820-024-01325-4>.
- [56] Y. Xu, L. Gao, L. Shen, Q. Liu, Y. Zhu, Q. Liu, L. Li, X. Kong, Y. Lu, H. Bin Wu, Ion-Transport-Rectifying Layer Enables Li-Metal Batteries with High Energy Density, *Matter* 3 (2020) 1685–1700, <https://doi.org/10.1016/j.matt.2020.08.011>.
- [57] S.K. Cho, K.S. Oh, J.C. Shin, J.E. Lee, K.M. Lee, J. Cho, W.B. Lee, S.K. Kwak, M. Lee, S.Y. Lee, Anion-rectifying polymeric single lithium-ion conductors, *Adv. Funct. Mater.* 32 (2022) 2107753, <https://doi.org/10.1002/adfm.202107753>.
- [58] R. Lin, Y. He, C. Wang, P. Zou, E. Hu, X.Q. Yang, K. Xu, H.L. Xin, Characterization of the structure and chemistry of the solid–electrolyte interface by cryo-EM leads to high-performance solid-state Li-metal batteries, *Nat. Nanotechnol.* 17 (2022) 768–776, <https://doi.org/10.1038/s41565-022-01148-7>.